Surface states and surface stability in half-metallic systems: the cases of zinc-blende-structure MnSb {111}A, {111}B and {001}

2007 J. Phys.: Condens. Matter 19 315214

(http://iopscience.iop.org/0953-8984/19/31/315214)

IOP PUBLISHING JOURNAL OF PHYSICS: CONDENSED MATTER

J. Phys.: Condens. Matter **19** (2007) 315214 (24pp) doi:10.1088/0953-8984/19/31/315214

Surface states and surface stability in half-metallic systems: the cases of zinc-blende-structure MnSb {111}A, {111}B and {001}

Sandro Mollet[1] **and Stephen J Jenkins**[2,3]

[1] Laboratorium für Physikalische Chemie, ETH Zürich, Switzerland
[2] Department of Chemistry, University of Cambridge, Lensfield Road, Cambridge CB2 1EW, UK

E-mail: sjj24@cam.ac.uk

Received 6 November 2006
Published 3 July 2007
Online at stacks.iop.org/JPhysCM/19/315214

Abstract

The surface properties of half-metallic materials can have a profound impact upon their possible utility for spintronic devices, and are therefore of significant interest. Here, we present the results of comprehensive density functional calculations for the {111}A, {111}B and {001} surfaces of the half-metallic zinc-blende phase of MnSb. We predict trimerized and dimerized reconstructions to be favourable whenever geometrically feasible, and our thermodynamic analysis strongly suggests termination with an Sb layer in all the cases studied. The electronic band-structure of the reconstructed Sb-terminated {001} surface is found to retain its half-metallicity, whereas the unfavourable Mn-terminated surface does not. The reconstructed Sb-terminated {111}A and {111}B surfaces are likewise half-metallic, and again the unfavourable Mn-terminated surfaces are not.

(Some figures in this article are in colour only in the electronic version)

Half-metals are ferromagnetic materials in which one spin species displays a metallic band-structure while the other is insulating; equivalently, a finite density of states exists at the Fermi level for just one of the two electronic spin channels [1]. Such a property, of course, carries significant implications for spin transport behaviour, and the possible uses of half-metallic materials in spintronic devices are consequently legion. Candidate spintronic half-metals include magnetite (Fe_3O_4), chromium dioxide (CrO_2), certain manganese perovskites (e.g. $La_{0.7}Sr_{0.3}MnO_3$), and some of the semi- and full-Heusler alloys (e.g. NiMnSb). More recently, a number of theoretical studies have suggested that certain V, Cr and Mn pnictides/chalcogenides may also show half-metallic properties when crystallized in particular

[3] Author to whom any correspondence should be addressed.

structures (see Pask *et al* [2], for instance). Nevertheless, considerable practical difficulties remain to be overcome before the potential of any of these materials can be realized; these have been discussed in a number of recent publications (see Dowben and Jenkins [3] for a review) and the detailed arguments need not be revisited here. In summary, however, one might note many-body issues, finite temperature effects, impurity scattering and segregation as critical problems related to half-metal bulk properties.

In addition to these bulk issues, however, it is also true that the surface and interface properties of half-metals give other causes for concern. Specifically, it is important to realize that even when the bulk properties of a material are perfectly half-metallic, and even when the surface or interface exhibits close-to-ideal stoichiometry and structure, it is entirely possible that surface- or interface-localized electronic states may exist that can radically affect spintronic properties within the selvedge [3–10]. Well documented examples include the minority-spin surface states of NiMnSb{111}A/B [6–8] and NiMnSb{001} [4, 7, 9, 10], which render the surface fully metallic because they cross the Fermi level. Furthermore, the minority-spin surface states of NiMnSb{001} at least are quite robust, as they persist when the surface is capped by several layers of Sb, essentially morphing from surface states into well localized interface states [5]. It is highly likely that similar interface states will be found in many cases, although some theoretical work does exist that suggests possible tactics for their avoidance [11, 12]. Although only having significant weight within a few angstroms of the surface or interface, it should be stressed that these states can have a crucial impact on the performance of spintronic devices, as they provide a channel for spin-flip scattering that can dominate the transport into or out of the half-metallic component [3].

In light of these considerations, it seems to us that it is essential to consider the electronic properties of surfaces and interfaces when assessing candidate spintronic materials. In the present work, we focus upon MnSb, a binary pnictide whose normal ground state phase (the NiAs, or $B8_1$, structure) is an ordinary ferromagnetic metal, but whose zinc-blende (B3) and wurtzite (B4) phases have been predicted to be half-metallic [2, 13, 14]. Specifically, we present results for the thermodynamic stability and electronic properties of the {111}A, {111}B and {001} surfaces of MnSb in the zinc-blende structure.

1. Theoretical methodology and calculated bulk properties

The results presented in this paper were obtained from calculations conducted within the CASTEP implementation of density functional theory [15]. In this particular scheme, wavefunctions are expanded in a basis set of plane waves and periodic boundary conditions are applied. For the bulk calculations this means that we need only represent the primitive unit cell explicitly, while for the surface calculations we must adopt a supercell geometry in which periodic images of our material slab are repeated in the surface-normal direction, separated by intervening vacuum regions The electron–ion interaction has been modelled throughout by means of ultrasoft pseudopotentials [16], with non-linear core corrections [17] included in the Mn case. Electronic exchange and correlation effects have been incorporated via the Perdew–Wang (PW91) form of the generalized gradient approximation (GGA) [18]. Further details of the precise methodology employed for individual calculations are provided below as appropriate.

1.1. MnSb in the zinc-blende (B3) structure

Our calculations for bulk MnSb in the zinc-blende structure were performed using a primitive unit cell (see table 1) and periodic boundary conditions. Wavefunctions were expanded in

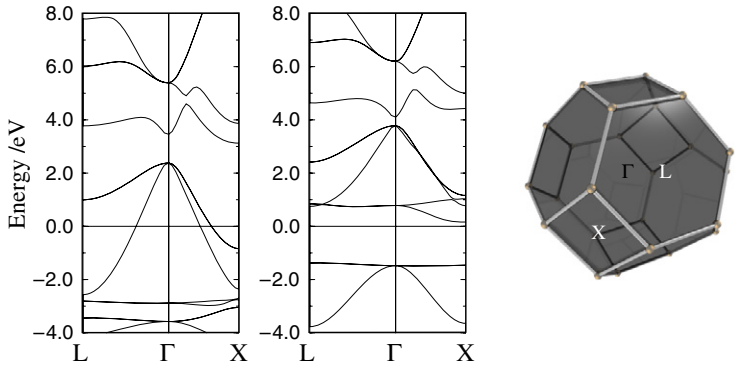

Figure 1. Band-structure and Brillouin zone of bulk MnSb in the zinc-blende (B3) structure, showing majority spin (left panel) and minority spin (right panel). The Fermi level is taken as the zero of energy.

a basis set of plane waves, up to a kinetic energy cut-off at 300 eV; integration over the Brillouin zone was accomplished via summation over a $5 \times 5 \times 5$ Monkhorst–Pack mesh [19]. Test calculations indicate that our results are well converged with respect to both of these parameters.

Upon optimization of the structure, the lattice constant was found to take a value of $a = 6.10$ Å, while the net spin magnetic moment per primitive cell was found to be 4.00 μ_B (see table 2). This latter fact is highly suggestive of half-metallicity[4]. To confirm this supposition, we have examined the **k**-resolved band-structure of zinc-blende MnSb, presented in figure 1. The majority-spin channel is seen to be unequivocally metallic in character, while the minority-spin channel displays a bandgap around the Fermi level of 1.54 eV; this bandgap is, however, asymmetrically located, so that the lowest unoccupied minority-spin states lie only 0.16 eV higher in energy than the highest occupied majority-spin states. These results are in good agreement with the preceding studies by Pask *et al* [2] and by Zheng and Davenport [13].

1.2. MnSb in the wurtzite (B4) structure

As a point of comparison for the zinc-blende structure, we also carried out calculations for MnSb in the wurtzite structure. We again utilized a plane wave cut-off at 300 eV, but the geometry of the primitive unit cell (see table 1) suggested a Monkhorst–Pack mesh of dimensions $5 \times 5 \times 3$ for Brillouin zone sampling. Again, larger meshes were considered in test calculations, but the choice cited here was found to yield well converged results.

Relaxation of the structure resulted in calculated lattice constants of $a = 4.38$ Å and $c = 7.02$ Å, with an internal parameter $u = 0.386$. The net spin magnetic moment per primitive unit cell was found to be 8.00 μ_B, once again raising the possibility of half-metallicity. Our calculated **k**-resolved band-structure (figure 2) clarifies this point, showing robust metallic behaviour for the majority-spin channel, together with a sizeable 1.45 eV bandgap for the minority-spin channel. As was found for the zinc-blende structure, this bandgap is asymmetrically offset with respect to the Fermi level, so that the lowest unoccupied minority-spin states lie only 0.23 eV higher in energy than the highest occupied majority-spin states. Again, these result are in good agreement with the existing theoretical literature [14].

[4] Note that the net spin moment per primitive unit cell of a half-metal must take an integer value. The reverse, however, is not *necessarily* true. That is, an integer spin moment may be the result of coincidence rather than half-metallicity.

Table 1. Calculated bulk structural parameters for MnSb in the B3 (zinc-blende), B4 (wurtzite) and $B8_1$ (NiAs) structures.

	Lattice	Atomic coordinates	Parameters
MnSb-B3	$a(0, 1, 1)/2$ $a(1, 0, 1)/2$ $a(1, 1, 0)/2$	Mn: (0, 0, 0) Sb: (1, 1, 1)/4	$a = 6.10$ Å
MnSb-B4	$a(\sqrt{3}, 1, 0)/2$ $a(-\sqrt{3}, 1, 0)/2$ $c(0, 0, 1)$	Mn: (0, 0, 0) Mn: (4, 2, 3)/6 Sb: $(0, 0, u)$ Sb: $(4, 2, 3 + 6u)/6$	$a = 4.38$ Å $c = 7.02$ Å $u = 0.386$
MnSb-$B8_1$	$a(\sqrt{3}, 1, 0)/2$ $a(-\sqrt{3}, 1, 0)/2$ $c(0, 0, 1)$	Mn: (0, 0, 0) Mn: (0, 0, 1)/2 Sb: (8, 4, 3)/12 Sb: (4, 8, 9)/12	$a = 4.01$ Å $c = 5.51$ Å

Table 2. Calculated bulk energies (in eV) and spin magnetic moments (in μ_B) per hetero-atomic pair of atoms for MnSb in the B3 (zinc-blende), B4 (wurtzite) and $B8_1$ (NiAs) structures.

	Energy	Spin moment
MnSb-B3	−809.05	4.00
MnSb-B4	−809.11	4.00
MnSb-$B8_1$	−810.00	3.03

The broad similarity between the band-structures of MnSb in the zinc-blende and wurtzite structures suggests that the half-metallic property is linked to the local tetrahedral bonding arrangement of the atoms (shared by both structures) and not to the long-range symmetry of the lattice (either cubic or hexagonal). This is promising in relation to the prospects of finding surface terminations that retain their half-metallicity, since it gives us no *a priori* reason to suppose that the surface's interruption of the ideal lattice symmetry should *necessarily* lead to highly dispersive, laterally delocalized surface states of the kind found on NiMnSb {111}A, {111}B and {001} [4–10]. On the other hand, the importance of short-range structure does imply the likelihood of mildly dispersive, laterally localized dangling-bond states for MnSb surfaces in both the zinc-blende and wurtzite structures. Calculations on the surfaces of wurtzite-structure MnSb will be deferred to a future publication [20], but the present work will show that such states are indeed characteristic of the zinc-blende-structure surfaces studied here.

1.3. MnSb in the NiAs ($B8_1$) structure

Although no surfaces of this phase are reported in the present work, it is worth re-emphasizing that it is the $B8_1$ (or NiAs) structure that represents the ground state for MnSb under standard conditions. For completeness, therefore, and to provide a reference energy to gauge the metastability of the zinc-blende and wurtzite phases, we include a brief discussion of the stable bulk structure at this juncture. Calculations in the NiAs structure were performed in a primitive unit cell (see table 1) with kinetic energy cut-off at 300 eV and a Monkhorst–Pack sampling mesh of dimensions $6 \times 6 \times 4$. The methodology and results here are essentially almost identical to those presented by one of us in an earlier work [6] (where some results for the {0001} surface

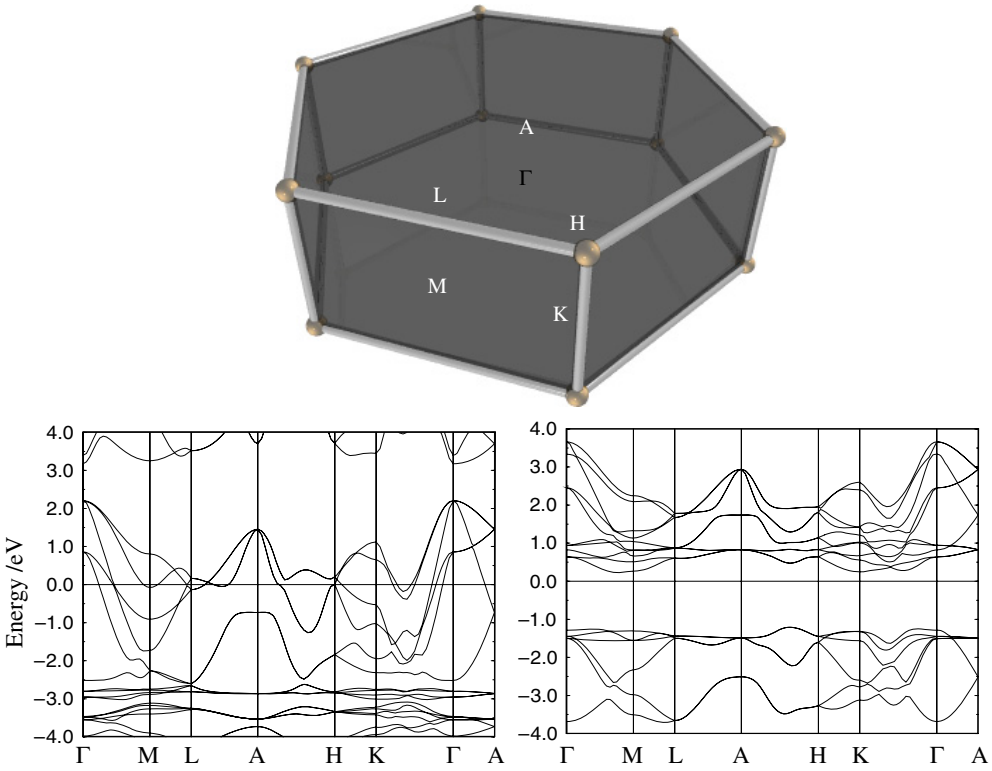

Figure 2. Band-structure and Brillouin zone of bulk MnSb in the wurtzite (B4) structure, showing majority spin (left panel) and minority spin (right panel). The Fermi level is taken as the zero of energy.

were also reported). The lattice constants and energy per primitive unit cell differ very slightly, due to the use of a denser **k**-point mesh in the present calculations.

Structural relaxation of the $B8_1$ phase produces lattice constants of $a = 4.01$ Å and $c = 5.51$ Å, with a net spin magnetic moment per primitive unit cell of 6.05 μ_B. Although this latter figure is *close* to an integer value, examination of the **k**-resolved band-structure (not shown) readily demonstrates that both majority-spin and minority-spin channels are robustly metallic.

2. Thermodynamic stability of bulk phases

Before discussing the stability of surface structures, it is vital first to set the scene by analysing the stability of the different bulk phases in some detail. To do so, we will adapt a rather useful form of triangular diagram employed previously by one of us to depict the thermodynamics of the semi-Heusler alloy NiMnSb [6, 7]. By rendering three coordinate axes within a two-dimensional space, the graph automatically respects some linear constraint that may be chosen for our convenience. In the case of the ternary alloy, the choice was that the chemical potentials of the three elements (μ_n, μ_m and μ_s for Ni, Mn and Sb respectively) summed to the bulk energy per primitive unit cell. Here, however, with only two elements present, we will instead

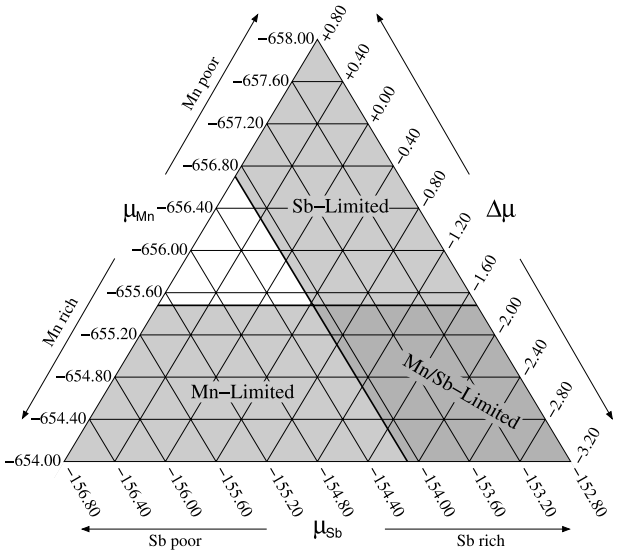

Figure 3. Generalized stability diagram for MnSb. The unshaded region represents absolute stability against segregation to the constituent elements. Shaded regions represent instability against segregation (see text for discussion of the Mn, Sb- and Mn/Sb-limited zones).

introduce a dummy potential, $\Delta\mu$, and insist that

$$\mu_{\mathrm{m}} + \mu_{\mathrm{s}} + \Delta\mu = \mu_{\mathrm{ms}}^{\mathrm{bulk}}, \tag{1}$$

where $\mu_{\mathrm{ms}}^{\mathrm{bulk}}$ is the chemical potential of bulk MnSb in its equilibrium ground state $B8_1$ structure. In accord with standard practice, we identify this quantity with the energy per hetero-atomic pair in a DFT calculation for the bulk material, thus obtaining a value of -810.00 eV. This allows us to construct the basic system of coordinate axes depicted in figure 3 and all other triangular plots included within the present work. Equation (1) is automatically satisfied as an inevitable consequence of the graphical representation we have employed; all acceptable combinations of chemical potential are present *somewhere* (and no unacceptable combinations may be found *anywhere*) on the graph.

Now equation (1) is, of course, simply a generalization of the usual equality,

$$\mu_{\mathrm{m}} + \mu_{\mathrm{s}} = \mu_{\mathrm{ms}}^{\mathrm{bulk}}, \tag{2}$$

that describes the relationship between the chemical potentials of individual species in equilibrium with the bulk ground state. The generalized equation clearly reduces to this more familiar case upon setting $\Delta\mu = 0$. The point of introducing the dummy potential is, however, that it allows one to treat systems in which the surface is in quasiequilibrium with a metastable bulk phase within essentially the same formalism. We begin by setting

$$\Delta\mu = \mu_{\mathrm{ms}}^{\mathrm{bulk}} - \mu_{\mathrm{ms}}, \tag{3}$$

in which μ_{ms} is an *effective* chemical potential for a (potentially) metastable bulk phase. That is, in the present case we identify μ_{ms} with the energy per hetero-atomic pair in zinc-blende-structure MnSb.

We next proceed by marking out the maximum values of μ_{m} and μ_{s} dictated by the bulk chemical potentials of Mn and Sb, according to the inequalities

$$\mu_{\mathrm{m}} \leqslant \mu_{\mathrm{m}}^{\mathrm{bulk}} \tag{4}$$

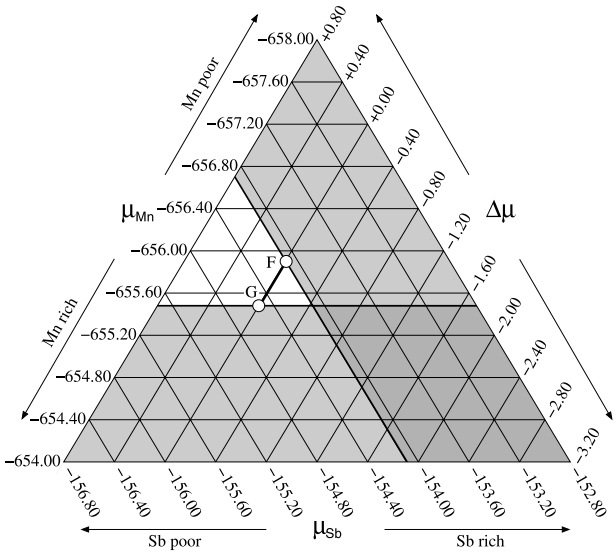

Figure 4. Stability diagram for MnSb in the $B8_1$ phase. The zone of absolute stability (unshaded region) is crossed by the line at $\Delta\mu = 0.00$ eV corresponding to the permitted chemical potentials for this phase; thermodynamically stable combinations are thus those lying on the line segment between points F and G.

and

$$\mu_s \leqslant \mu_s^{\text{bulk}} \tag{5}$$

in which the values of μ_m^{bulk} and μ_s^{bulk} are just the energies per atom in the bulk elemental materials, and are taken from an earlier paper to be -645.49 and -154.12 eV respectively [6]. Bulk phases of MnSb are therefore only thermodynamically favourable against segregation into Mn and Sb for combinations of chemical potentials lying within the unshaded region of figure 3, which we now describe as the 'zone of absolute stability' (although note that this zone extends beyond the arbitrarily chosen upper-left boundary of the graph as depicted).

In contrast, the 'Sb-limited zone of instability' corresponds to the case where the Mn-related inequality is satisfied but the Sb-related inequality is not, and the 'Mn-limited zone of instability' corresponds to the situation where the Sb-related inequality is satisfied but the Mn-related inequality is not; these two regions are shaded mid grey in figure 3. Finally, the region where neither inequality is satisfied is labelled the 'Mn/Sb-limited zone of instability', and shaded dark grey in the figure. In the Sb-limited zone, it is *only* the strong preference for a pure Sb phase that drives segregation, while in the Mn-limited zone it is *only* the strong preference for a pure Mn phase that is the driving force. In the Mn/Sb-limited phase, the excess stability of *either one* of the two pure elements would alone be sufficient to drive segregation.

Now, to investigate the stability of MnSb in the ground state $B8_1$ phase, we need only set $\Delta\mu = 0$ and read off the chemical potentials along that line on the triangular graph. It is immediately apparent that the line corresponding to $\Delta\mu = 0$ does indeed pass through the zone of absolute stability. Thus the chemical potentials found on the line segment between F and G in figure 4 are possible combinations consistent with the existence of stable bulk MnSb in the $B8_1$ phase.

For MnSb in the zinc-blende phase, however, our calculations yield $\mu_{ms} = -809.05$ eV, so that we must look at the line corresponding to $\Delta\mu = -0.95$ eV. Doing so, we find that

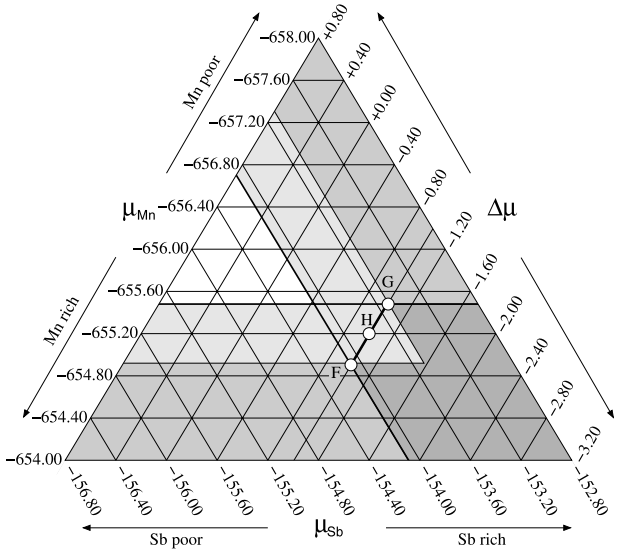

Figure 5. Stability diagram for MnSb in the zinc-blende phase. The zone of absolute stability (unshaded region) is not crossed by the line at $\Delta\mu = -1.00$ eV corresponding to permitted chemical potentials for this phase. There are thus no combinations of chemical potentials corresponding to true thermodynamic stability against elemental segregation for zinc-blende-structure MnSb. An illustrative zone of metastability has been shaded light grey on the periphery of the zone of absolute stability, according to criteria described in the text.

this line does not enter the zone of absolute stability at all (see figure 5). That is, not only will the zinc-blende phase be unstable with respect to the $B8_1$ phase, it is actually unstable even with respect to segregation into separate Mn and Sb phases. All points along this line are equally unstable with respect to $B8_1$, while the point of minimum instability with respect to the separated elements is represented by the point of closest approach to the zone of absolute stability, i.e. point H in figure 5. Under conditions when the zinc-blende structure can exist as a metastable phase, however, we know that at least this single point must lie sufficiently close to the zone of absolute stability that the kinetic barrier against segregation is high enough to prevent a phase transition[5]. In reality, it is feasible that some *range* of points close to H may, in fact, also be metastable. For illustrative purposes, we have highlighted in figure 5 the line segment lying between the Mn-limited and Sb-limited zones of instability (i.e. between points F and G), and have indicated a putative 'zone of metastability' with boundaries parallel to those of the zone of absolute stability and just large enough to encompass these points. That is to say, *if* the points lying within the zone of metastability constitute the entire set of points close enough to the zone of absolute stability to avoid a phase transition, *then* the points lying on the line segment between F and G would represent all combinations of chemical potentials consistent with metastable MnSb in the zinc-blende structure. Note that we do not *actually* know precisely how large the zone of metastability should be under a given set of conditions (i.e. temperature, ambient concentration of Mn- or Sb-bearing species, etc), although a width of around 0.6 eV, as drawn, does not seem to us entirely unreasonable as a ballpark estimate.

[5] In light of the Brønsted–Evans–Polanyi relation [21, 22], we expect kinetic barriers to be somewhat proportional to the change in enthalpy involved in the phase transition. The closer a metastable phase lies to the zone of absolute stability, the smaller the thermodynamic driving force towards restructuring (i.e. the smaller the enthalpy differential between the metastable and fully segregated states) and hence the larger the kinetic barrier.

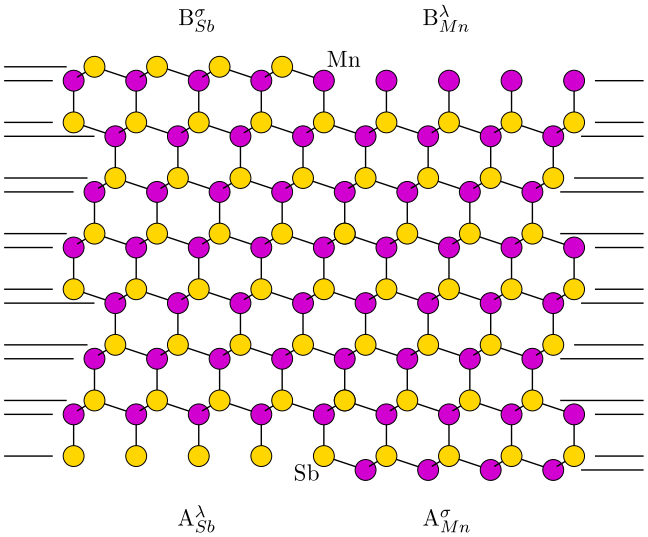

Figure 6. Side-view schematic diagram of the MnSb{111}A and MnSb{111}B surface terminations.

3. Surfaces in the zinc-blende structure

The four high-symmetry surfaces of zinc-blende materials are {001}, {111}A, {111}B and {110}. Of these, the {111}A, {111}B and {001} cases are relatively simple in their structure, exposing only a single chemical species in each unreconstructed atomic plane. The {110} surface has a more complex structure, in which each atomic plane features atoms of both species, and the possibilities for non-stoichiometric configurations are consequently rather greater. For the present work, we have chosen to focus upon only the {111}A, {111}B and {001} surfaces; the {110} surface will be described in a future publication [23]. We note, at this juncture, that a small number of calculations have been reported in the literature for the surfaces of certain half-metallic zinc-blende-structure materials (namely CrAs{001} [24], VSe{001} [25], CrSe{001} [25], VAs{001} [25], MnAs{001} [25], CrS{001} [26] and CrP{110} [27]) but neither relaxation nor reconstruction appear to have been considered in any of these studies. One very recent calculation for CrAs{110} [28] *does* include relaxation, but again no reconstruction, or indeed variation in surface stoichiometry. As we shall see below, however, both surface reconstruction *and* stoichiometry can have a significant impact on the electronic properties of such surfaces, and certainly ought not to be neglected.

3.1. The MnSb{111}A and MnSb{111}B surfaces

For MnSb{111}A and MnSb{111}B surfaces in the zinc-blende phase, we begin with calculations for the unreconstructed (1 × 1) surfaces, which we classify according to the chemical species in the uppermost layer and to the final interlayer spacing[6]. In total, four unreconstructed terminations may be enumerated (see figure 6), which may be grouped into two pairs: (A) on one side of the slab, it is possible to terminate the surface with a plane of Sb atoms and a long final interlayer spacing, or to terminate the surface with a plane of Mn atoms and a

[6] The {111} planes of zinc-blende alternate in chemical identity from one layer to the next, while the spacing *between* them alternates between short and long values.

Table 3. Calculated supercell energies ($E(X)$ in eV) for MnSb{111}A and MnSb{111}B surfaces (X denotes the character of the surface that is allowed to relax in each case). The parameters n_m and n_s respectively represent the number of Mn and Sb atoms present within the supercell in each case. The total supercell length was always equivalent to 14 atomic layers.

X	Periodicity	Reconstruction	n_m	n_s	$E(X)$
A^{λ}_{Sb}	(1×1)	None	4	4	−3232.97
A^{σ}_{Mn}	(1×1)	None	4	3	−3079.65
B^{λ}_{Mn}	(1×1)	None	4	4	−3232.73
B^{σ}_{Sb}	(1×1)	None	3	4	−2579.38
A^{λ}_{Sb}	$(\sqrt{3} \times \sqrt{3})$	None	12	12	−9698.25
A^{σ}_{Mn}	$(\sqrt{3} \times \sqrt{3})$	None	12	9	−9238.56
B^{λ}_{Mn}	$(\sqrt{3} \times \sqrt{3})$	None	12	12	−9697.86
B^{σ}_{Sb}	$(\sqrt{3} \times \sqrt{3})$	None	9	12	−7737.72
A^{λ}_{Sb}	$(\sqrt{3} \times \sqrt{3})$	Trimer	12	12	−9701.09
A^{σ}_{Mn}	$(\sqrt{3} \times \sqrt{3})$	Triad	12	9	−9238.61
B^{λ}_{Mn}	$(\sqrt{3} \times \sqrt{3})$	Trimer	12	12	−9699.35
B^{σ}_{Sb}	$(\sqrt{3} \times \sqrt{3})$	Triad	9	12	−7737.72

short final interlayer spacing, and (B) on the *other* side of the slab, it is possible to terminate the surface with a plane of Mn atoms and a long final interlayer spacing, or to terminate the surface with a plane of Sb atoms and a short final interlayer spacing. We will employ the superscripts σ and λ to indicate surfaces terminating with short and long interlayer spacings respectively [29], and utilize chemical symbols as subscripts to indicate the identity of the top-layer atoms. Thus, the two terminations of the 'A' side of the slab may be denoted A^{λ}_{Sb} and A^{σ}_{Mn}, while those of the 'B' side are B^{λ}_{Mn} and B^{σ}_{Sb}.[7] Note that the energetic differential between the 'A' side and the 'B' side is not accessible from a slab calculation, because it is impossible to create a slab that does not possess *both* an 'A' *and* a 'B' side. This differential is, however, important only in dictating matters such as the macroscopic shape of crystallites and *which* surface planes will be dominant, not in understanding the microscopic issue of which termination is exposed at each individual surface. It is *not* possible for an 'A' surface to rearrange itself into a 'B' surface, or vice versa, without an associated change in the macroscopic crystal shape. On the other hand, it *is* incisive for the surface scientist to ask whether A^{λ}_{Sb} is more or less stable than A^{σ}_{Mn}, or indeed whether B^{λ}_{Mn} is more or less favoured than B^{σ}_{Sb}, since the answers to these questions will indeed dictate the microscopic physical character of the exposed surface.

In order to tackle these issues, it is necessary to somehow deal with the 'A' and 'B' sides of the slab separately. We achieve this from the baseline of an eight-layer slab constructed to feature A^{λ}_{Sb} termination on one side and B^{λ}_{Mn} termination on the other. First keeping the latter side of the slab frozen in the bulk geometry, we perform a DFT calculation in which the

[7] The existing notation for labelling zinc-blende surfaces is less than fully satisfactory. Strictly speaking, in accordance with formal crystallographic convention, the symbol {111} indicates only the set of symmetry-related surfaces (111), $(1\bar{1}\bar{1})$, $(\bar{1}1\bar{1})$, and $(\bar{1}\bar{1}1)$, while the complementary surfaces $(\bar{1}\bar{1}\bar{1})$, $(\bar{1}11)$, $(1\bar{1}1)$, and $(11\bar{1})$ should be indicated by, for example, $\{11\bar{1}\}$. In practice, the literature usually refers instead to the (111)A surface, when what is meant is *any one* of the strictly {111} surfaces, and to the (111)B surface when what is meant is *any one* of the strictly $\{11\bar{1}\}$ surfaces (ironically, not including the (111) surface, of course). Ideally, our notation ought therefore to distinguish $\{111\}^{\lambda}_{Sb}$ and $\{111\}^{\sigma}_{Mn}$ on one side of the slab, with $\{11\bar{1}\}^{\lambda}_{Mn}$ and $\{11\bar{1}\}^{\sigma}_{Sb}$ on the other, where the symbols {111} and $\{11\bar{1}\}$ retain their formal crystallographic meaning. In the interests of simplicity, and of making contact with the more familiar notation, we choose to adopt the convention that {111}A is *colloquially* equivalent to the formal meaning of {111}, while {111}B is equivalent to the formal meaning of $\{11\bar{1}\}$. We may thus assert the notational equivalences $A^{\lambda}_{Sb} \equiv \{111\}^{\lambda}_{Sb}$, $A^{\sigma}_{Mn} \equiv \{111\}^{\sigma}_{Mn}$, $B^{\lambda}_{Mn} \equiv \{11\bar{1}\}^{\lambda}_{Mn}$, and $B^{\sigma}_{Sb} \equiv \{11\bar{1}\}^{\sigma}_{Sb}$.

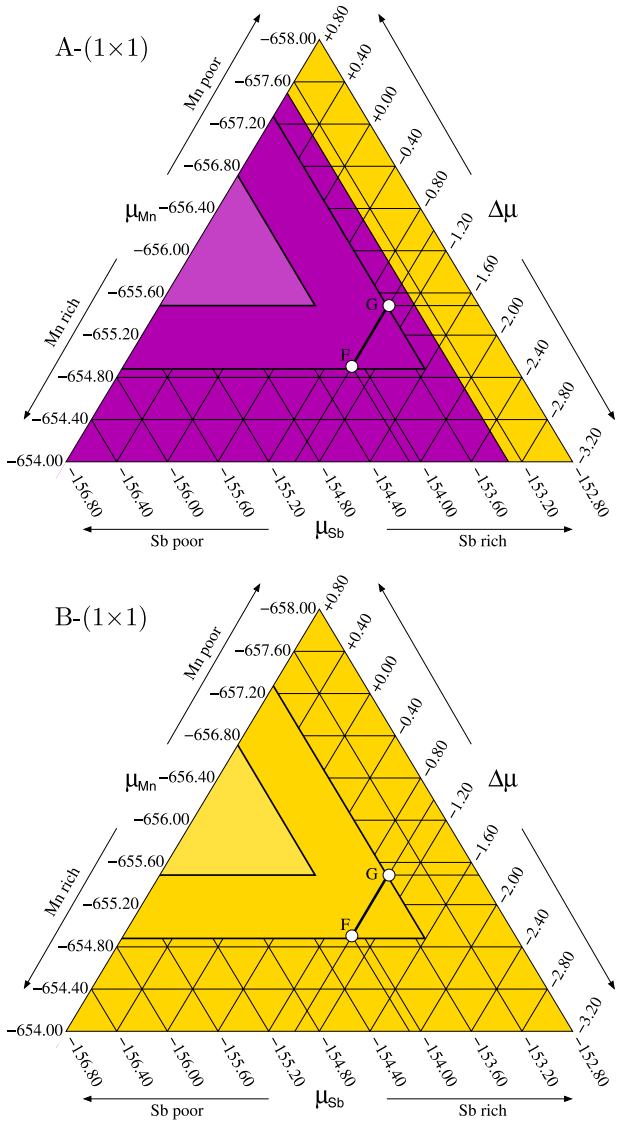

Figure 7. Stability diagrams for the (1 × 1) MnSb{111}A and MnSb{111}B surfaces (upper and lower panels, respectively). In each case, the triangles with grid-lines suppressed correspond to the zones of absolute stability and of metastability depicted in figure 5. In these, and all similar diagrams presented here, regions shaded in yellow (light) are those for which the Sb termination is favoured, while those shaded in purple (dark) indicate Mn termination favoured.

A^{λ}_{Sb} side is allowed to relax (to a depth of four layers), obtaining an energy per supercell (or 'supercell energy') that we designate $E(A^{\lambda}_{Sb})$. Next, we remove one layer of atoms from the 'A' side, and allow the surface to relax again (this time to a depth of three layers), obtaining the supercell energy designated $E(A^{\sigma}_{Mn})$. Freezing the back surface of the slab ensures that, to a very good approximation, the *difference* in these two energies is solely due to the changes effected at the 'A' surface. In a similar manner, we then perform two further calculations with the 'A' side frozen in its bulk-terminated A^{λ}_{Sb} geometry, in which the 'B' side is allowed to relax

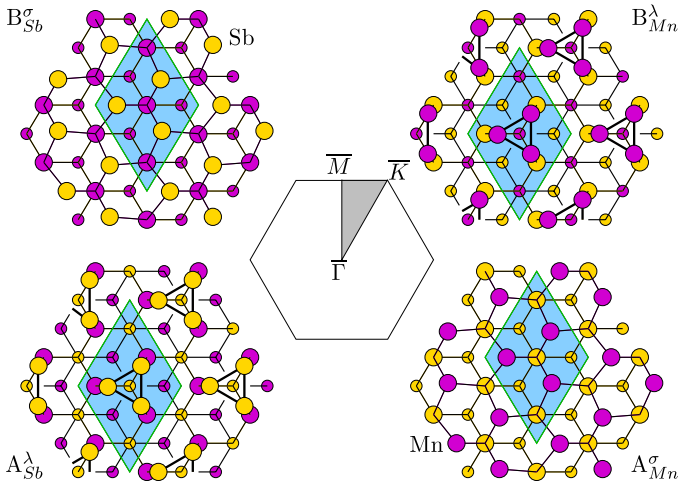

Figure 8. Top-down schematic diagrams of primitive unit cells and the corresponding Brillouin zone for the $(\sqrt{3} \times \sqrt{3})$ surfaces of MnSb{111}A and MnSb{111}B, including the labelling scheme for high-symmetry points. The unit cell depicted in each case is centred on either a trimer or a contracted triad, as appropriate.

in either the B^{λ}_{Mn} termination (to a depth of four layers) or the B^{σ}_{Sb} termination (to a depth of three layers), yielding the supercell energies $E(B^{\lambda}_{Mn})$ and $E(B^{\sigma}_{Sb})$ respectively. The calculated energies are summarized in table 3.

Now, it ought to be clear that the energies $E(A^{\lambda}_{Sb})$ and $E(A^{\sigma}_{Mn})$ cannot simply be compared in order to determine which of these terminations is most favourable, since the calculations that produced them contained differing numbers of atoms (specifically, the latter supercell contained one Sb atom fewer than the former). Likewise, the energies $E(B^{\lambda}_{Mn})$ and $E(B^{\sigma}_{Sb})$ cannot be directly compared either, for essentially the same reason (the latter supercell containing one Mn atom fewer than the former). To cope with this, it is necessary to compare not the internal energy emerging from DFT, but instead to consider a thermodynamic potential (or 'free energy') appropriate to systems with variable particle number (and in our case, fixed temperature, entropy, volume, and pressure). The necessary quantities take the form:

$$F = E - n_{\mathrm{m}}\mu_{\mathrm{m}} - n_{\mathrm{s}}\mu_{\mathrm{s}} \tag{6}$$

where the values of E are just those supercell energies alluded to above, the integers n_{m} and n_{s} are respectively the numbers of Mn and Sb atoms appearing in the supercell used for the calculation, and μ_{m} and μ_{s} are respectively the chemical potentials of Mn and Sb atoms. Once these latter two quantities are known, one may then simply compare the free energies $F(A^{\lambda}_{Sb})$ and $F(A^{\sigma}_{Mn})$ to determine the preferred termination of the 'A' side, and similarly comparison of $F(B^{\lambda}_{Mn})$ with $F(B^{\sigma}_{Sb})$ will reveal the equivalent information for the 'B' side.

We proceed graphically by evaluating equation (6) for each pair of chemical potentials lying within the triangular plot of figure 5, and shading the diagram according to the favoured surface termination. That is, taking the 'A' side as our first example, if $F(A^{\sigma}_{Mn})$ is lower than $F(A^{\lambda}_{Sb})$ for some pair of chemical potentials μ_{m} and μ_{s}, then that point in the graph will be shaded purple (representing termination by Mn); if the opposite were true, then that point would be shaded yellow instead (representing termination by Sb). A similar procedure is, of course, also followed for the 'B' side. It is then possible to read off from the graph which of the

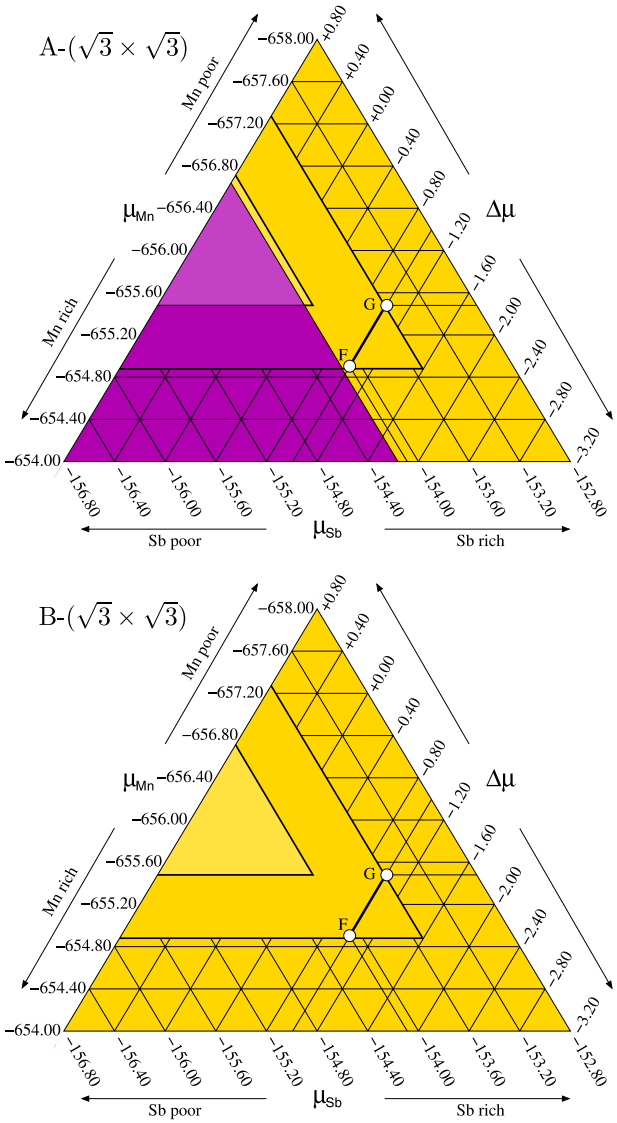

Figure 9. Stability diagrams for the ($\sqrt{3} \times \sqrt{3}$) MnSb{111}A and MnSb{111}B surfaces (upper and lower panels, respectively). See figure 7 for guide to interpretation.

terminations is favoured for the line segment lying between points F and G, representing the combinations of chemical potential most consistent with MnSb in the metastable zinc-blende structure.

In the case of the two 'B' surfaces, there is a clear preference for the B^{σ}_{Sb} termination over the B^{λ}_{Mn} termination, whereas for the 'A' surfaces it is the A^{σ}_{Mn} termination that is favoured over the A^{λ}_{Sb} termination (see figure 7). That is, despite the apparent preference for Sb termination noted in an earlier work on NiMnSb and related compounds [6], the preference for σ termination over λ termination appears here to be stronger. It is vitally important to recall, however, that these results correspond only to the unreconstructed (1×1) surface.

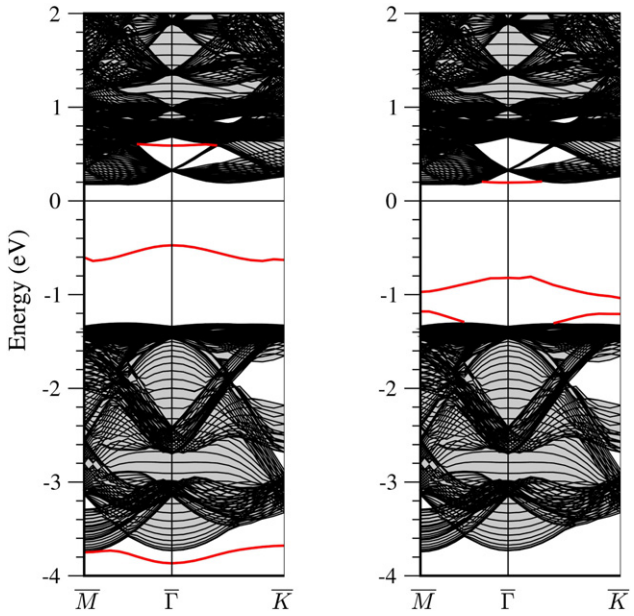

Figure 10. Minority-spin band-structures for the $(\sqrt{3} \times \sqrt{3})$ MnSb{111}A and MnSb{111}B surfaces. Bands within the shaded regions are projections of the bulk band-structure onto the surface Brillouin zone, while bands lying outside the shaded regions correspond to true surface-localized states. The Fermi level is taken as the energy zero. Both panels show bands within the Brillouin zone appropriate to a $(\sqrt{3} \times \sqrt{3})$ surface unit cell. The left-hand panel depicts the bands for the A^{λ}_{Sb} termination, while the right-hand panel shows the B^{σ}_{Sb} termination.

Whilst an exhaustive survey of possible surface reconstructions for zinc-blende-structure MnSb{111}A and MnSb{111}B is beyond the scope of the present work, we have nevertheless investigated plausible possibilities based upon a $(\sqrt{3} \times \sqrt{3})$ unit cell; these are illustrated schematically in figure 8. In the case of the A^{λ}_{Sb} and B^{λ}_{Mn} terminations, such a periodicity allows the formation of *trimers* in the uppermost layer. At the A^{σ}_{Mn} and B^{σ}_{Sb} surfaces, the rigidity of the atoms in the uppermost layer (bound as they are to three underlying atoms each) prevents any really significant lateral movement, although some slight displacement does nevertheless occur; for want of a more appropriate terminology, we describe such displacements as forming contracted *triads*, and note that the associated energy drop was found to be modest or negligible (0.05 eV per triad for A^{σ}_{Mn}, and 0.00 eV per triad for B^{σ}_{Sb}). For surfaces forming trimers, however, the energetic preference was much stronger, amounting to 2.84 eV per trimer (0.95 eV per (1×1) cell) for the A^{λ}_{Sb} termination and 1.49 eV per trimer (0.50 eV per (1×1) cell) for the B^{λ}_{Mn} termination. After adjusting the free energies to account for these reconstructions, we find that the extra flexibility associated with the λ termination allows the A^{λ}_{Sb} termination to become slightly more favourable than A^{σ}_{Mn} (see figure 9). Although it is possible that more complex reconstructions than these simple $(\sqrt{3} \times \sqrt{3})$ examples may occur in reality, it is quite likely that these too will involve trimerization or triadic displacements, and that overall it will be the Sb terminated surfaces that are typically most stable.

Looking in detail at the **k**-resolved minority-spin band-structure of the B^{σ}_{Sb} termination (figure 10, right-hand panel) we immediately recognize several distinct surface states, three occupied and two unoccupied. The lowest of the occupied bands crosses into the bulk continuum in the vicinity of the $\overline{\Gamma}$ point, but rises to around -1.2 eV towards the zone edge;

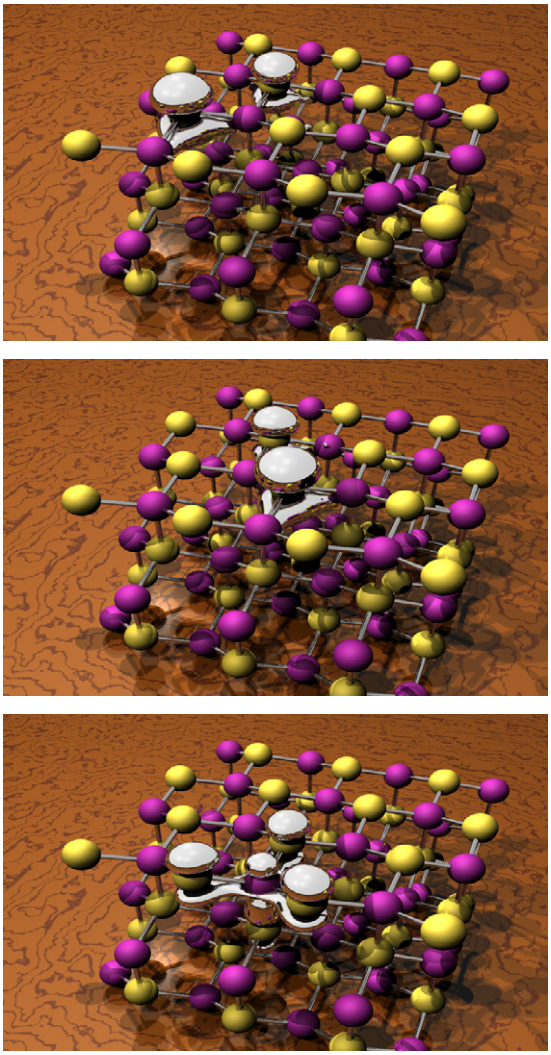

Figure 11. Occupied minority-spin surface states of the Sb-terminated MnSb{111}B surface (B^{σ}_{Sb}). The upper and middle panels show the square moduli of the doubly degenerate primarily p_z-derived e wavefunctions (-0.82 eV @ $\overline{\Gamma}$), and the lower panel the same for the p_z/d_{z^2}-derived a_1 wavefunction (-1.20 eV @ $\overline{K}$). In these and all other similar depictions within the present work, the isosurface is drawn at a threshold of 1.0×10^{-2} e Å^{-3} and only the contribution from within a single primitive unit cell of the reconstructed surface is shown.

the other pair of states is degenerate and reaches a rather flat maximum around -0.8 eV at the zone centre. The non-degenerate occupied state derives from an a_1 bonding combination[8] of Sb p_z orbitals with second-layer Mn d_{z^2} orbitals; the degenerate pair comprises e states, deriving predominantly from Sb p_z orbitals (see figure 11). The two unoccupied states derive from Mn

[8] We note that there are three distinct threefold rotational axes per primitive unit cell for each of the reconstructed {111}A or {111}B surfaces. For the purposes of assigning symmetry labels to electronic states, we must consider our origin to lie at some point along *one* of these axes, but recognize that *any* of them would be an acceptable choice so long as applied consistently. To avoid ambiguity, we will always choose the axis passing through the centre of the trimer or triad.

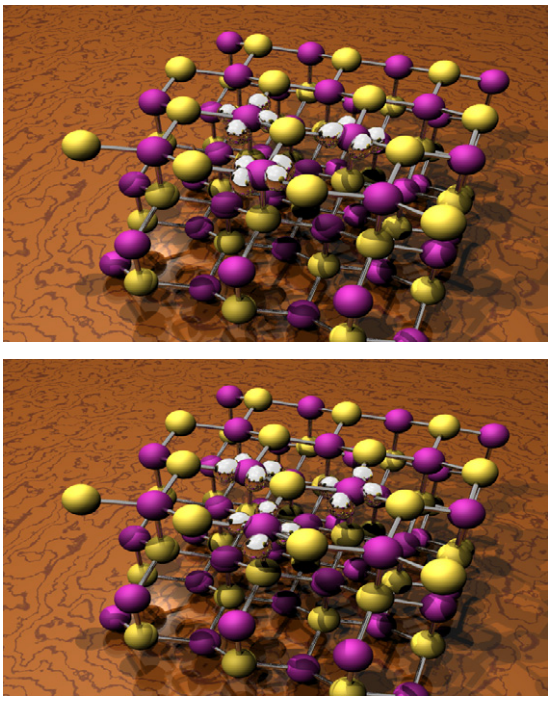

Figure 12. Unoccupied minority-spin surface states of the Sb-terminated MnSb{111}B surface (B^{σ}_{Sb}). The panels show square moduli of the doubly degenerate d_{ij}-derived e wavefunctions (0.19 eV @ $\overline{\Gamma}$).

d orbitals and form another degenerate pair, lying around 0.2 eV above the Fermi level close to the zone centre (figure 12).

Turning to the band-structure of the A^{λ}_{Sb} termination (figure 10, left-hand panel) we see that although the surface states are qualitatively somewhat similar to those we have just described their energies are radically different. In particular, the formation of a compact trimer is associated with the a_1 surface state here being situated around 3.8 eV below the Fermi level, indicating rather strong bonding between the Sb p_z orbitals; once again, there is also a degenerate pair of occupied e states deriving from the Sb p_z orbitals, but these lie slightly higher than those of the B^{σ}_{Sb} termination, at around -0.5 eV (see figure 13). A single unoccupied a_2 state deriving from second-layer Mn d orbitals is found in the vicinity of the zone centre at approximately 0.6 eV above the Fermi level (figure 14).

Significantly, both of the favoured surface terminations (A^{λ}_{Sb} and B^{σ}_{Sb}) are robustly half-metallic, with no minority-spin surface states approaching within around 0.2 eV of the Fermi level from above and 0.5 eV from below. Such a situation can occur here (whereas it does not in the cases of NiMnSb {111}A, {111}B and {001} for example) because the surface states are all essentially dangling-bond-like, with consequently somewhat limited dispersion. Interestingly, the band-structures of the disfavoured A^{σ}_{Mn} and B^{λ}_{Mn} terminations feature highly dispersive surface states and are *not* half-metallic.

3.2. The MnSb{001} surface

For MnSb{001} in the zinc-blende phase, we first carried out calculations for the unreconstructed (1×1) surface in both Mn-terminated and Sb-terminated structures (the two

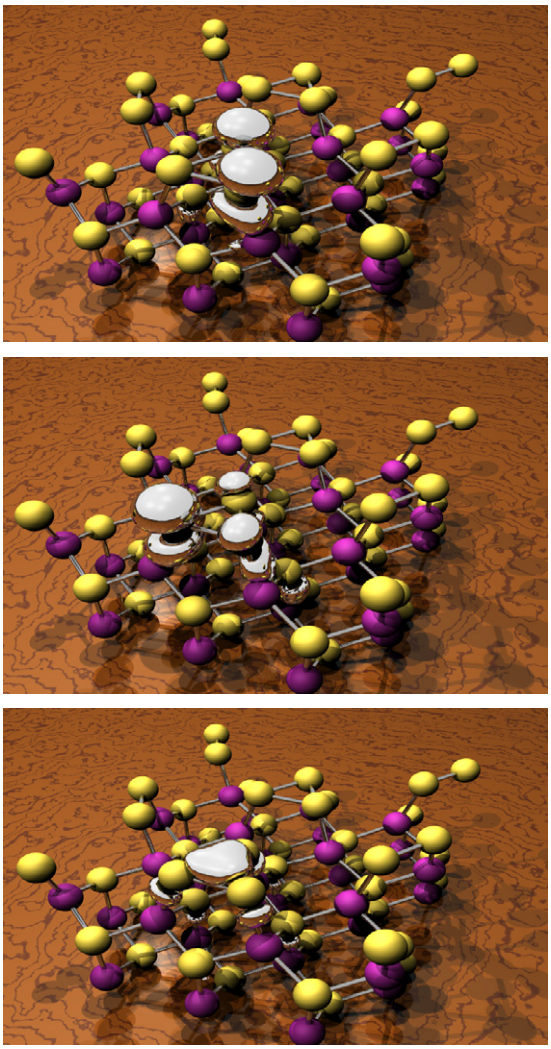

Figure 13. Occupied minority-spin surface states of the trimerized Sb-terminated MnSb{111}A surface (A^{λ}_{Sb}). The upper and middle panels show the square moduli of the doubly degenerate p_z-derived e wavefunctions (-0.47 eV @ $\overline{\Gamma}$), and the lower panel the same for the p_z-derived a_1 wavefunction (-3.87 eV @ $\overline{\Gamma}$).

are interrelated by the addition or removal of a single layer of atoms). The Mn-terminated calculations involved five layers of Mn and four of Sb, and vice versa for the Sb-terminated calculations; in each case, both sides of the slab were allowed to relax to a depth of three layers, so that they remain equivalent and the analysis of energetics is simplified. We denote the energies thus obtained $E({}^{d}X_{Mn})$ and $E({}^{d}X_{Sb})$ for the Mn- and Sb-terminated slabs respectively (see table 4). Figure 15 (upper panel), constructed according to the same scheme as discussed in the preceding subsection, clearly shows that Sb termination is preferred when no surface reconstruction is allowed.

In order to investigate possible *dimer* reconstruction of the surface, however, we also carried out calculations within a (2×1) unit cell (see figure 16). Here, we utilized a thinner

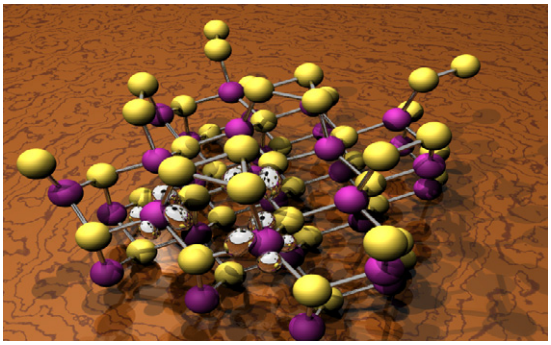

Figure 14. Unoccupied minority-spin surface state of the Sb-terminated MnSb{111}A surface (A^{λ}_{Sb}). The panel shows the square modulus of the d_{ij}-derived a_2 wavefunction (0.58 eV @ $\overline{\Gamma}$).

Table 4. Calculated supercell energies ($E(X)$ in eV) for MnSb{001} surfaces (X denotes the character of the surface that is allowed to relax in each case, and the prefix 'd' indicates a 'double-sided' calculation where *both* sides of the slab are identical and allowed to relax). The parameters n_m and n_s respectively represent the number of Mn and Sb atoms present within the supercell in each case. The total supercell length was always equivalent to 16 atomic layers.

X	Periodicity	Reconstruction	n_m	n_s	$E(X)$
$^{d}X_{Mn}$	(1×1)	None	5	4	−3888.46
$^{d}X_{Sb}$	(1×1)	None	4	5	−3388.41
X_{Mn}	(2×1)	None	6	6	−4849.68
X_{Sb}	(2×1)	None	6	6	−4849.89
X_{Mn}	(2×1)	Dimer	6	6	−4850.33
X_{Sb}	(2×1)	Dimer	6	6	−4850.64

slab (six layers in total, instead of nine) with only one side relaxed (to a depth of three layers) for reasons of computational economy. The difference between the Mn-terminated and Sb-terminated calculations is then simply the matter of which side was allowed to relax, in much the same manner as for the {111}A and {111}B surfaces dealt with in the preceding section. This approach complicates the analysis of energetics and electronic structure, since each calculation involves not only a contribution from the physical relaxed surface, but also one from the unphysical unrelaxed back surface. It does not, however, compromise accuracy so long as the slab is not taken too thin; in our case the slab thickness remained suitable for our purpose. Energies for the Mn-terminated and Sb-terminated slabs (i.e. with either the Mn-terminated side or the Sb-terminated side allowed to relax) are presented in table 4 as $E(X_{Mn})$ and $E(X_{Sb})$. From *these* results, we can conclude that dimerization is favourable for both terminations, yielding a stabilization energy of 0.65 eV per dimer for the Mn-terminated surface, and of 0.75 eV per dimer for the Sb-terminated surface. These energies clearly *increase* the relative stability of the Sb-terminated surface over that of the Mn termination, albeit by only a small amount (see figure 15, lower panel).

Examining the detailed **k**-resolved minority-spin band-structures of the two terminations is rather instructive (see figure 17). Concentrating first upon the Mn termination (upper panels) we plot the surface states of both the non-dimerized and dimerized geometries within the Brillouin zone appropriate to the (2×1) unit cell. For the non-dimerized case, two surface states are found within the minority-spin fundamental gap; both cross the Fermi level, rendering the

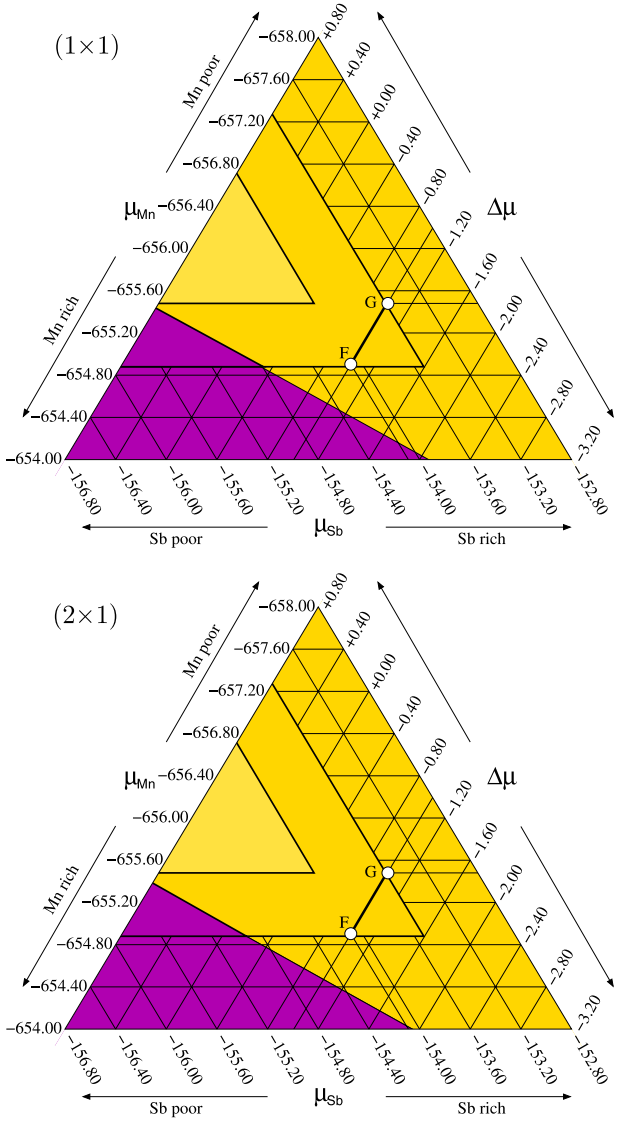

Figure 15. Stability diagram for the MnSb{001} surface (the upper panel shows the unreconstructed surface, the lower panel the dimerized surface). See figure 7 for a guide to interpretation.

surface region fully metallic rather than half-metallic. On formation of the Mn–Mn dimer, one of these states drops to around 0.6 eV below the Fermi level, but the other remains largely unaffected by the change in geometry, and the metallicity of the surface is thus preserved.

For the Sb termination, however, the picture is quite different (figure 17, lower panels). Four distinct surface states are found in the non-dimerized geometry. The highest lying of these reaches a maximum at the $\overline{\Gamma}$ point, around 0.3 eV below the Fermi level, and is primarily composed of an antibonding combination of p_x orbitals located on the top-layer Sb atoms (see figure 16 for our coordinate convention). A bonding combination of Sb p_x orbitals constitutes the surface state found close to the valence band edge throughout the zone and degenerate

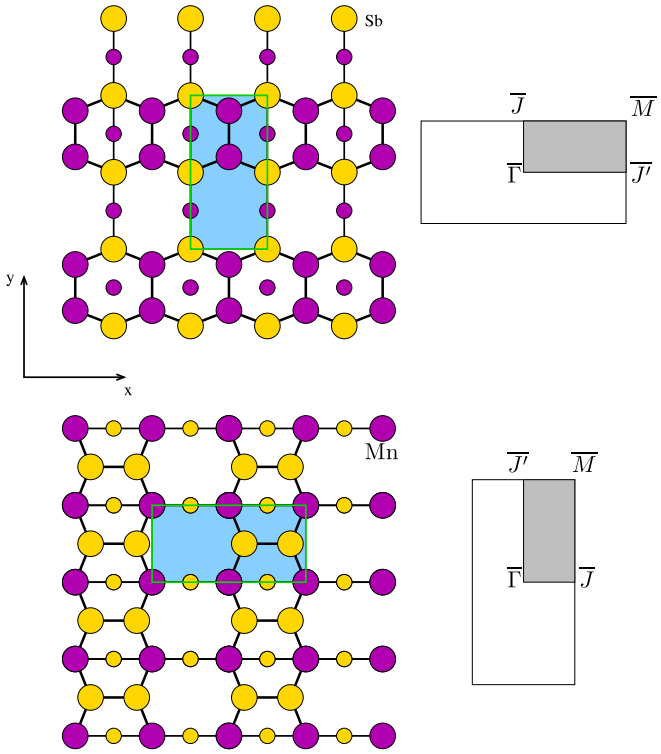

Figure 16. Top-down schematic diagrams of primitive unit cells and corresponding Brillouin zones for the (2×1) dimerized surfaces of MnSb{001}, showing the conventions adopted for Cartesian axes and labelling of high-symmetry points.

with the other p_x-derived state at the $\overline{J}$ point. The remaining two surface states, found in the fundamental gap in the vicinity of the $\overline{J'}$ point, are of Sb p_z character, the upper one being a bonding combination and the lower antibonding. Upon formation of the Sb–Sb dimer, the antibonding p_x-related state is pushed up in energy out of the fundamental gap, where it ceases to exist as a well defined surface state. The p_x-derived σ-bonding a_1 state[9], on the other hand, drops in energy down to around -2.8 eV, where it retains a distinct surface character within a small stomach gap close to the $\overline{J'}$ point (figure 18, middle panel). The shift in the p_z-derived states is smaller than either of these, but results in both emerging fully into the fundamental gap, with the π-antibonding b_1 combination settling on average about 0.3 eV higher in energy than the π-bonding a_1 combination (figure 19). An entirely new surface state, of p_y-derived π-bonding b_2 character, is located just below the bottom of the valence band (figure 18, lower panel), and another, of p_y-derived π-antibonding a_2 character, is found just above the top of the valence band (figure 18, upper panel). Overall, the surface remains half-metallic.

It is rather interesting to note, in passing, just how similar the electronic structure of the dimerized Sb-terminated surface is to that found for group V elements on diamond structure substrates. In particular, the pair of occupied p_z-related states is a common feature [30–33]; moreover, the *ordering* of the p_z-derived π-bonding/antibonding combinations displays a

[9] In assigning symmetry labels for the reconstructed {001} surface, we note that there are four distinct twofold rotational axes per primitive unit cell, upon *either* of which the origin might conveniently be considered to lie; we choose always the one passing through the centre of a dimer bond.

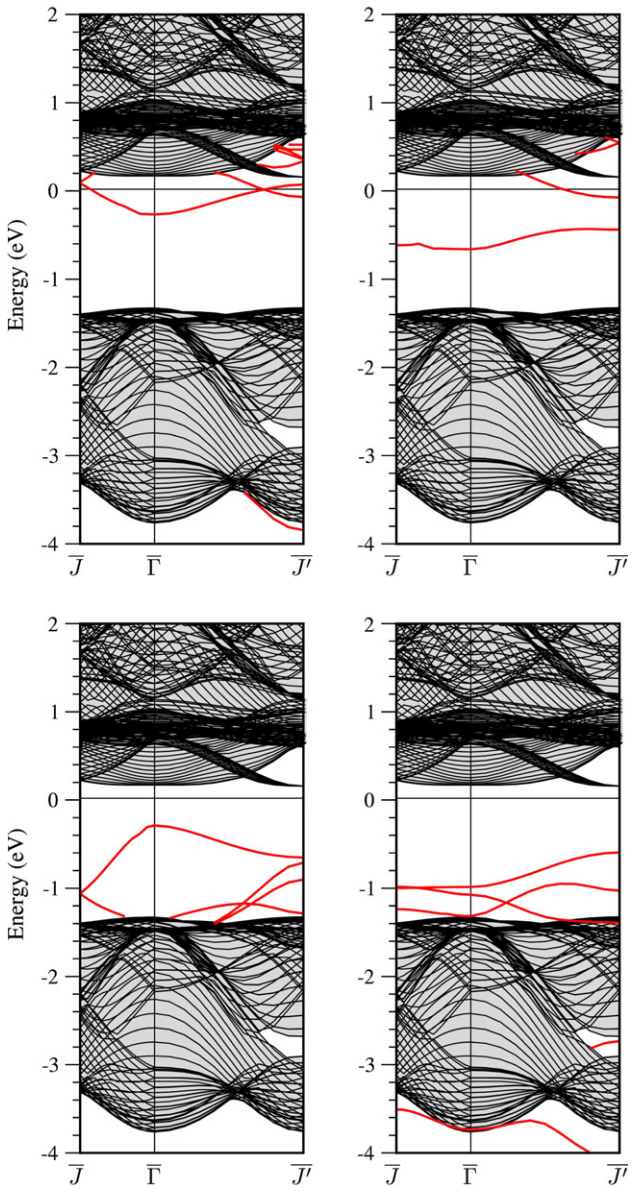

Figure 17. Minority-spin band-structures for the MnSb{001} surface. Bands within the shaded regions are projections of the bulk band-structure onto the surface Brillouin zone, while bands lying outside the shaded regions correspond to true surface-localized states. The Fermi level is taken as the energy zero. All panels show bands within the Brillouin zone appropriate to a (2×1) surface unit cell. The upper panels depict the bands for the unreconstructed (left) and dimer-reconstructed (right) Mn-terminated surfaces, while the lower panels show the bands for the unreconstructed (left) and dimer-reconstructed (right) Sb-terminated surfaces.

marked trend with respect to the bond length, with the bonding state lying much lower than the antibonding for Si{001}/P, slightly lower for Si{001}/As, slightly higher for Si{001}/Sb and much higher for Si{001}/Bi [34]. Despite the fact that the present work deals with Sb dimers, it is worth pointing out that the Sb–Sb dimer length of 2.69 Å found here is actually much *shorter*

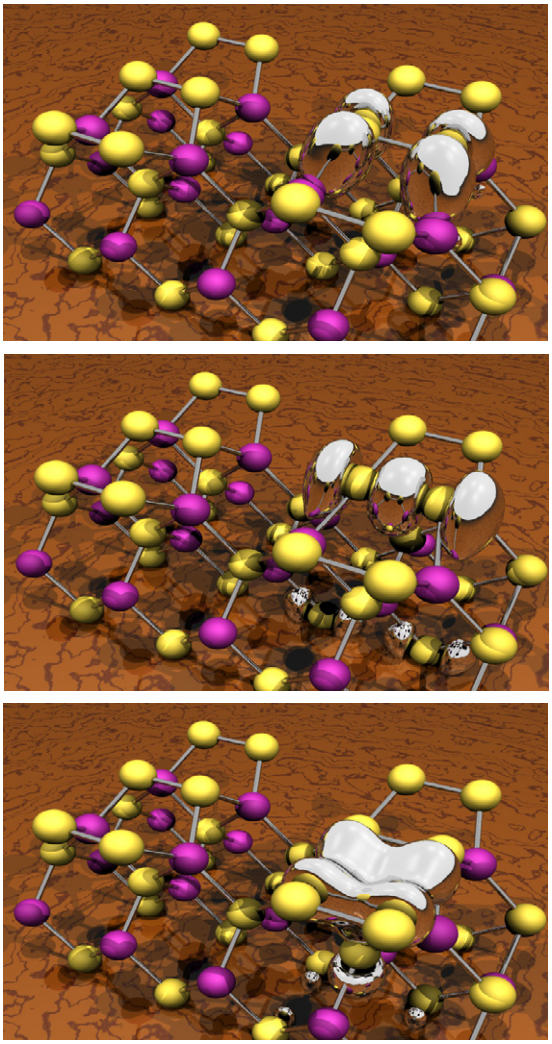

Figure 18. Minority-spin surface states of the dimerized Sb-terminated MnSb{001} surface. The upper panel shows the square modulus of the p_y-derived π-antibonding a_2 wavefunction (-1.07 eV @ $\overline{\Gamma}$), the middle panel the same for the p_x-derived σ-bonding a_1 wavefunction (-2.75 eV @ $\overline{J'}$), and the lower panel the same again for the p_y-derived π-bonding b_2 wavefunction (-4.07 eV @ $\overline{J'}$). It is worth noting that the comparatively delocalized nature of this latter state in the y-direction is reflected in its having the strongest dispersion of all the minority-spin surface states, along the $\overline{\Gamma J'}$ axis of the Brillouin zone.

than the value of 2.96 Å found for dimers of the same element on the Si{001} substrate, in line with the observation that the bonding combination in the present case lies slightly *below* the antibonding.

4. Conclusions

In this work, we have calculated the first detailed, momentum-resolved electronic band-structures for surfaces of a zinc-blende half-metal. Also for the first time, we have done so whilst including the effects of realistic relaxation and reconstruction. For the {111}A, {111}B

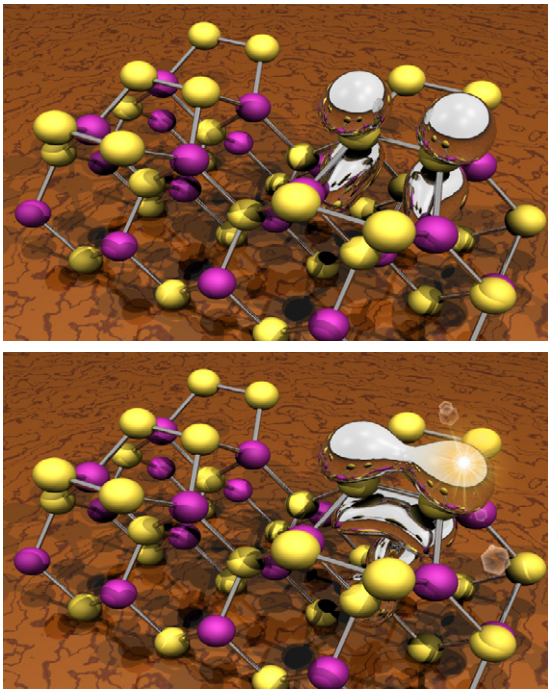

Figure 19. Minority-spin surface states of the dimerized Sb-terminated MnSb{001} surface. The upper panel shows the square modulus of the p_z-derived π-antibonding b_1 wavefunction (-0.60 eV @ $\overline{\Gamma}$), and the lower panel the same for the p_z-derived π-bonding a_1 wavefunction (-1.03 eV @ $\overline{\Gamma}$).

and {001} surfaces of MnSb, we have shown that termination by the anion is favoured in all cases examined, and that reconstruction by trimerization or dimerization (to reduce the number of dangling bonds) is a general feature, so long as sufficient flexibility exists in the backbonds to allow significant lateral displacements in the outermost atomic layer. Reconstruction has a profound effect upon the electronic properties of these surfaces, clearly implying that it is *essential* to include this possibility in any future calculations of this type. For all the favoured terminations obtained in the present study, the minority-spin surface states are typically found to have relatively little dispersion (the p_y π-bonding state of the dimerized anion-terminated {001} surface being the only real exception) and *all* of these cases retain half-metallicity at the surface. The unfavourable cation-terminated surfaces, on the other hand, do not. Although we have studied only MnSb as an archetype, we firmly believe that the surface band-structures of other zinc-blende half-metals will display very similar qualitative features.

Acknowledgments

We are grateful for an Erasmus Scholarship (SM) and for a Royal Society University Research Fellowship (SJJ). Dr Stephanie Pratt is warmly thanked for helpful discussions concerning the nature of zinc-blende surface terminations.

References

[1] de Groot R A, Mueller F M, van Engen P G and Buschow K H J 1983 *Phys. Rev. Lett.* **50** 2024
[2] Pask J E, Yang L H, Fong C Y, Pickett W E and Dag S 2003 *Phys. Rev.* B **67** 224420

[3] Dowben P A and Jenkins S J 2005 *Frontiers in Magnetic Materials* ed A Narlikar (Berlin: Springer)
[4] Jenkins S J and King D A 2001 *Surf. Sci. Lett.* **494** L793
[5] Jenkins S J and King D A 2002 *Surf. Sci. Lett.* **501** L185
[6] Jenkins S J 2004 *Phys. Rev.* B **70** 245401
[7] Jenkins S J 2005 *Local-Moment Ferromagnets: Unique Properties for Modern Applications* ed M Donath and W Nolting (Berlin: Springer)
[8] Lezaic M, Galanakis I, Bihlmayer G and Blügel S 2005 *J. Phys.: Condens. Matter* **17** 3121
[9] Lezaic M, Mavropoulos P, Bihlmayer G and Blügel S 2006 *J. Phys. D: Appl. Phys.* **39** 797
[10] Correa J S, Eibl C, Rangelov G, Braun J and Donath M 2006 *Phys. Rev.* B **73** 125316
[11] de Wijs G A and de Groot R A 2004 *Phys. Rev.* B **64** 020402
[12] Attema J J, de Wijs G A and de Groot R A 2006 *J. Phys. D: Appl. Phys.* **39** 793
[13] Zheng J-C and Davenport J W 2005 *Phys. Rev.* B **69** 144415
[14] Xie W-H, Liu B-G and Pettifor D G 2003 *Phys. Rev.* B **68** 134407
[15] CASTEP 4.2 academic version, licensed under the UKCP-MSI agreement; Payne M C, Teter M P, Allan D C, Arias T A and Joannopoulos J D 1992 *Rev. Mod. Phys.* **64** 1045
[16] Vanderbilt D 1990 *Phys. Rev.* B **41** 7892
[17] Louie S G, Froyen S and Cohen M L 1982 *Phys. Rev.* B **26** 1738
[18] Perdew J P, Chevary J A, Vosko S H, Jackson K A, Pederson M R, Singh D J and Fiolhais C 1992 *Phys. Rev.* B **46** 6671
[19] Monkhorst H J and Pack J D 1976 *Phys. Rev.* B **13** 5188
[20] Mollet S and Jenkins S J 2007 in preparation
[21] Brønsted N 1928 *Chem. Rev.* **5** 231
[22] Evans M G and Polanyi N P 1936 *Trans. Faraday Soc.* **32** 1333
[23] Mollet S and Jenkins S J 2007 in preparation
[24] Galanakis I 2002 *Phys. Rev.* B **66** 012406
[25] Galanakis I and Mavropoulos P 2003 *Phys. Rev.* B **67** 104417
[26] Byun Y, Lee J I and Jang Y-R 2006 *J. Appl. Phys.* **99** 08J101
[27] Lee J I, Byun Y and Jang Y-R 2006 *Surf. Sci.* **600** 1608
[28] Lee J I and Hong S C 2006 *IEEE Trans. Magn.* **42** 2936
[29] Jenkins S J and Pratt S J 2006 *Surf. Sci. Rep.* submitted
[30] Jenkins S J and Srivastava G P 1996 *Surf. Sci.* **352–354** 411
[31] Jenkins S J and Srivastava G P 1997 *Phys. Rev.* B **56** 9221
[32] Jenkins S J and Srivastava G P 1997 *Surf. Sci. Lett.* **384** L886
[33] Gay S C A, Jenkins S J and Srivastava G P 1998 *Surf. Sci.* **404** 641
[34] Gay S C A, Jenkins S J and Srivastava G P 1998 *J. Phys.: Condens. Matter* **10** 7751